Characterization of the defect density states in MoO$_x$ for c-Si solar cell applications

Scirè, D.; Macaluso, Robert; Mosca, Mauro; Mirabella, S. ; Gulino, Antonino; Isabella, O.; Zeman, M.; Crupi, I.

Important note
To cite this publication, please use the final published version (if applicable).
Please check the document version above.

Characterization of the defect density states in MoOx for c-Si solar cell applications

D. Scirè[1]*, R. Macaluso[1], M. Mosca[1], S. Mirabella[2], A. Gulino[3], O. Isabella[4], M. Zeman[4], I. Crupi[1]

[1] Department of Engineering, University of Palermo, Palermo, Italy
[2] Department of Physics and Astronomy, University of Catania, Catania, Italy
[3] Department of Chemical Sciences, University of Catania, Catania, Italy
[4] Photovoltaic Materials and Devices group, Delft University of Technology, Delft, the Netherland
*Addrress correspondence to: daniele.scire@unipa.it

Abstract

Thin layers of MoOx have been deposited by thermal evaporation followed by post-deposition annealing. The density of states distributions of the MoOx films were extracted deconvoluting the absorption spectra, measured by a photothermal deflection spectroscopy setup, including the small polaron contribution. Results revealed a sub-band defect distribution centered 1.1 eV below the conduction band; the amplitude of this distribution was found to increase with post-deposition annealing temperature and film thickness.

Keywords

c-Si solar cell, photovoltaic, transition metal oxide, molybdenum oxide, density of states, small polaron.

1. Introduction

Silicon-based heterojunction technology (HJT) is one of the most promising candidates for high performance and low-cost solar cells with world-record efficiency close to 27% in interdigitated back contact architecture [1]. The HJT exploits the excellent passivation properties of hydrogenated amorphous silicon (a-Si:H), although the use of doped a-Si:H has drawbacks such as parasitic absorption and low-thermal budget to cope with back-end metallization.

Replacing the p-type a-Si:H with a doping-free transition metal oxide (TMO) such as molybdenum oxide (MoOx), is a viable alternative allowing conversion efficiency up to 23.5% [2] rivaling the traditional contact despite its lower level of optimization. Moreover, the hole selectivity capability of the MoOx is exploited for other classes of electronic devices such as organic light-emitting diodes [3], organic photovoltaic cells [4], thin-film solar cells [5]. Thus, the optimization of this hole-selective layer has been investigated over the past years, highlighting the role of the defect density of states (DOS) [6–8]. Nonetheless, information on the DOS, linked to oxygen vacancies [9], lacks for TMOs.

We aim to fill this gap by providing insights into the MoOx defect density needed for accurate simulation and optimization of HJT solar cells with this TMO as a hole-selective contact. Therefore, chemical, morphological and optical characterizations were conducted on thin films of MoOx. Finally, the DOS of MoOx samples were extracted from the deconvolution of the absorption spectra [10,11], including the absorption related to excitation of electrons from small polaron states filled by electron transfer from the oxygen vacancies. A systematic study of the effects of both layers thickness and post-deposition annealing (PDA) treatments on the extracted DOS is furthermore presented.

2. Experimental

Thin films of molybdenum oxide were deposited by thermal evaporation on quartz substrates with desired thicknesses of 20, 50 and 100 nm. After deposition, the layers were annealed at different temperatures (T_{PDA} from 100 to 250 °C) for 30 minutes in ambient air. The desired thickness of the samples was confirmed by ex-situ ellipsometry and Rutherford backscattering spectrometry (RBS) which did not show , as displayed in Fig. 1, any significant variation between as-deposited and annealed samples.
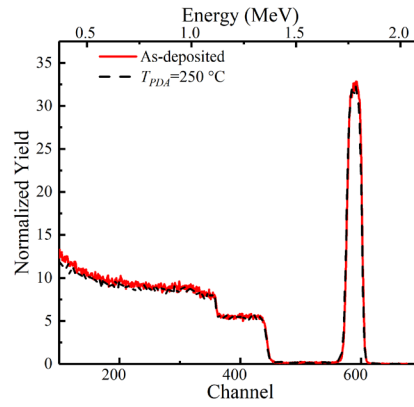
Fig. 1: RBS spectrum of the 20 nm MoO$_x$ samples as-deposited and after annealing at 250°C for 30 minutes.

The structure and morphology of the samples were investigated through Raman spectroscopy and Scanning Electron Microscopy, respectively. The measurements show that all the samples were amorphous, independently on the PDA and the thickness, with no significant surface morphology variation. The chemical composition was studied by X-ray photoelectron spectroscopy (XPS). The optical properties were analyzed through ellipsometry and photothermal deflection spectroscopy (PDS).

3. Results

The Mo 3d binding region is presented in Fig. 2. From XPS measurement, the presence of a doublet structure with a spin-orbit separation of 3.0 eV is highlighted. The Mo 3d level is deconvoluted with two doublet components, a dominating one associated with the presence of Mo^{6+} [12] and a weak doublet shifted 2 eV to lower energy indicating the presence of Mo^{5+} (linked to the oxygen vacancies) [12].
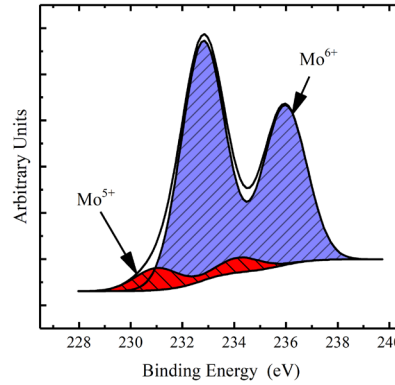

Fig.2: XPS spectrum of the Mo 3d binding region.

The absorption spectra, presented in Fig 3, decay exponentially from lower wavelength to a valley at about 490 nm and then rises to a peak around 900 nm. There are no significant differences between the curves in the wavelength range of 350-400 nm; while the peak observed in the Vis-NIR range tendentially grows as the annealing temperature rises. This increase in the absorption is referred to MoO$_x$ reduction in the annealed samples. Interestingly, for the 20 nm thick MoO$_x$ films (Fig. 3a), the spectra of the samples annealed at 200°C and 250 °C have a comparable magnitude, whilst, for the higher thicknesses, such behavior is less evident. Furthermore, for the 50 nm thick samples (Fig. 3b), the spectrum of the sample annealed at 100°C is similar to the as-deposited one; for the 100 nm case (Fig. 3c), such behavior is more evident since the as-deposited sample presents a spectrum higher than the sample annealed at 100°C.
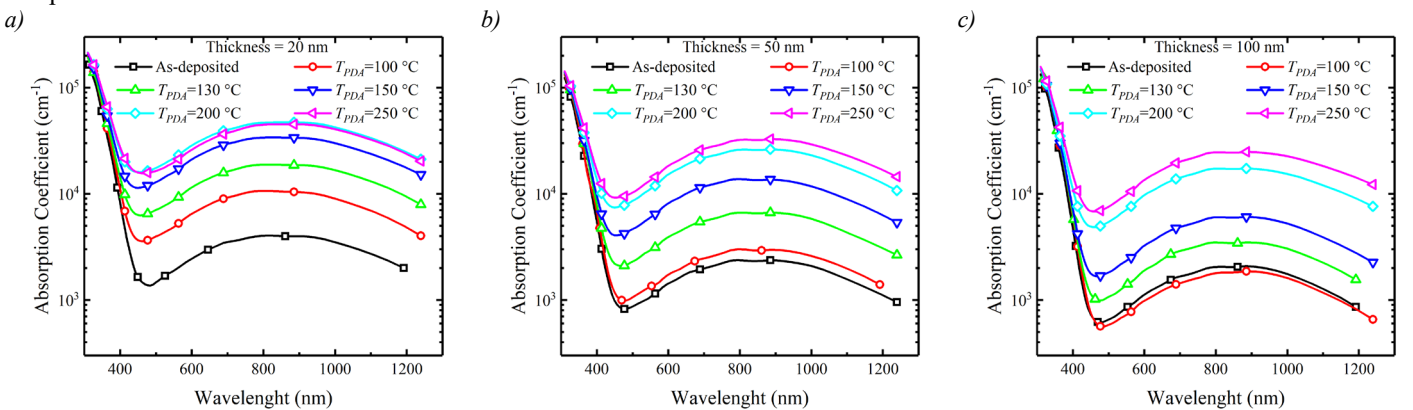
a) b) c)

Fig.3: Absorption spectrum of a) 20 nm, b) 50 nm, c) 100 nm thick MoOx films as deposited and after different PDA

4. Model and discussion

The density of states of the MoO$_x$ was described as the superposition of different distributions, assuming parabolic distribution for the valence and conduction bands (N_{VB}, N_{CB}), exponential distribution for the valence and conduction band tails (N_{VBT}, N_{CBT}), and Gaussian distribution for the defects states in the bandgap (N_D) [11]:

$$DOS(E) \rightarrow \begin{cases} N_{VB}(E) = N_V\sqrt{-E + E_G + E_{0V}} & E < 0 \\[2mm] N_{CB}(E) = N_C\sqrt{E - E_{0C}} & E \geq 0 \\[2mm] N_{VBT}(E) = N_V\sqrt{\dfrac{E_{0V}}{2}}\ \exp\left(-\dfrac{E + E_G}{E_{0V}}\right) & E > E_G \\[2mm] N_{CBT}(E) = N_C\sqrt{\dfrac{E_{0C}}{2}}\exp\left(\dfrac{E}{E_{0C}}\right) & E < 0 \\[2mm] N_D(E) = \dfrac{A_D}{\sqrt{2\pi W^2}}\exp\left[-\dfrac{1}{2}\left(\dfrac{E + E_D}{W}\right)^2\right] & E_G < E < 0 \end{cases} \tag{1}$$

with E energy (the zero-energy reference was considered at the edge of the conduction band), E_{0V} and E_{0C} valence and conduction band tails, E_G energy gap; for Gaussian defect distribution: A_D area, E_D mean position and W the FWHM. The densities of states of the valence (N_V) and conduction (N_C) band were 7.92×10^{17} cm^{-3}eV$^{-3/2}$ and 6.78×10^{18} cm^{-3}eV$^{-3/2}$, respectively [11].

The peaks in the absorption spectra are attributed to the small polaron [13,14], a quasi-particle describing the interaction of a trapped electron with the surrounding atoms [14,15]. Furthermore, small polaron is a typical feature of TMOs [13,16–19].

Therefore, to achieve the best fit of the absorption spectra, we introduce an additive term in the set of equations (1) to consider the polaron contribution. The polaron absorption, α_p function of the photon energy ($h\nu$), is modeled with a weakly asymmetric Gaussian peak [11,13,18]:

$$\alpha_p(h\nu) = \frac{A_p}{h\nu}\exp\left(-\frac{\left(h\nu - 2E_p\right)^2}{8E_p\,E_{op}}\right) \tag{2}$$

with A_p polaron pre-exponential factor, E_p polaron binding energy, and E_{op} longitudinal-optical phonon energy. The values of the DOS distributions were extracted through the absorption spectra α fitting through the one-electron approximation and including the polaron absorption α_p [11]:

$$\alpha(h\nu) = \frac{C}{h\nu}\int N_i(E)F(E)N_f(E + h\nu)[1 - F(E + h\nu)]dE + a_p(h\nu) \tag{3}$$

where N_i and N_f are the initial and final states, F is the Fermi-Dirac function. The constant C was calibrated at 4 eV resulting 4.13·10^{-31} cm^5·eV^2 [11]. The obtained DOS lays about 1.1 eV below the conduction band edge with an amplitude rising with both T_{PDA} and film thickness (Fig. 4a). Interestingly, the defect distribution amplitude rises as the thickness is reduced and for increasing T_{PDA}. A similar trend was found for the A_P (Fig. 4b), whilst the other parameters of the small polaron remained fixed.

The resulting coefficients are summarized in Table 1 and are limited for brevity to the 100 nm thick samples.

Table 1: Defect distributions and small polaron coefficients at different T_{PDA} for the 100 nm thick samples

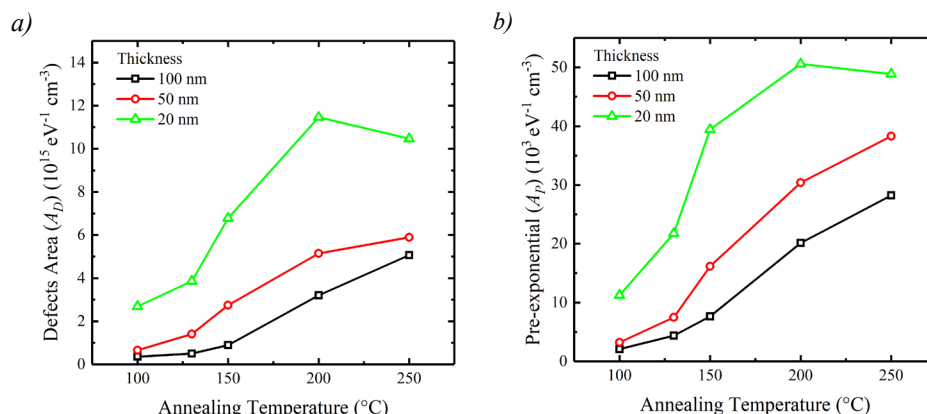| T_{PDA} (°C)	Thickness (nm)	E_{0V} (meV)	E_{0C} (meV)	A_D (ev^{-1}cm^{-3})	E_D (eV)	W (eV)	A_P (ev^{-1}cm^{-3})	E_P (eV)	E_{op} (meV)
As. dep.	100	100	141	3.41 × 10^{14}	1.14	0.05	2.46 × 10^3	0.80	52.5
100	100	117	191	3.61 × 10^{14}	1.16	0.05	2.10 × 10^3	0.78	43.9
130	100	115	269	5.07 × 10^{14}	1.18	0.05	4.39 × 10^3	0.81	52.2
150	100	118	243	8.89 × 10^{14}	1.18	0.05	7.67 × 10^3	0.80	52.5
200	100	128	182	3.21 × 10^{15}	1.15	0.05	2.01 × 10^4	0.79	55.8
250	100	83	101	5.07 × 10^{15}	1.11	0.05	2.82 × 10^4	0.77	54.6

Fig.4: Defects area (a) and polaron pre-exponential factor (b) against annealing temperature for different MoO$_x$ films thicknesses

5. Conclusion

Thin films of MoO$_x$ were synthesized by thermal evaporation, subsequentely annealed, and then characterized to provide an insight into the DOS. The deconvolution of the absorption spectra resulted in a defect DOS distribution centered 1.1 eV below the conduction band edge with its amplitude increasing against both T_{PDA} and film thickness. The small polaron parameters, extrapolated from the optical measurements, revealed that both binding and longitudinal-optical phonon energy are independent of the thickness and the T_{PDA}, whilst the pre-exponential factor exhibits a similar trend to the amplitude of the defect distribution. The DOS characterization here employed for MoO$_x$ films has shown to be a valuable method to determine the DOS and could be easily extended to other TMOs currently exploited as carrier selective contacts in solar cells.

References

[1] Yoshikawa K, Kawasaki H, Yoshida W, Irie T, Konishi K, Nakano K, et al. Silicon heterojunction solar cell with interdigitated back contacts for a photoconversion efficiency over 26%. Nat Energy 2017;2. https://doi.org/10.1038/nenergy.2017.32.

[2] Dréon J, Jeangros Q, Cattin J, Haschke J, Antognini L, Ballif C, et al. 23.5%-Efficient Silicon Heterojunction Silicon Solar Cell Using Molybdenum Oxide As Hole-Selective Contact. Nano Energy 2020;70. https://doi.org/10.1016/j.nanoen.2020.104495.

[3] Xue Q, Liu S, Zhang S, Chen P, Zhao Y, Liu S. Improved performances of organic light-emitting diodes with mixed layer and metal oxide as anode buffer. Solid State Electron 2013;79:75–8. https://doi.org/10.1016/j.sse.2012.05.066.

[4] Chang FK, Huang YC, Jeng JS, Chen JS. Band offset of vanadium-doped molybdenum oxide hole transport layer in organic photovoltaics. Solid State Electron 2016;122:18–22. https://doi.org/10.1016/j.sse.2016.04.014.

[5] Salomé PMP, Vermang B, Ribeiro-Andrade R, Teixeira JP, Cunha JMV, Mendes MJ, et al. Passivation of Interfaces in Thin Film Solar Cells: Understanding the Effects of a Nanostructured Rear Point Contact Layer. Adv Mater Interfaces 2018;5:1–10. https://doi.org/10.1002/admi.201701101.

[6] Scire D, Bonadonna M, Zhao Y, Procel P, Isabella O, Zeman M, et al. Analysis of Transition Metal Oxides based Heterojunction Solar Cells with S-shaped J-V curves. 12th AEIT Int. Annu. Conf. AEIT 2020, IEEE; 2020, p. 1–6. https://doi.org/10.23919/AEIT50178.2020.9241142.

[7] Hao LC, Zhang M, Ni M, Liu JM, Feng XD. Simulation of high efficiency silicon heterojunction solar cells with molybdenum oxide carrier selective layer. Mater Res Express 2018;5. https://doi.org/10.1088/2053-1591/aace80.

[8] Mazzarella L, Alcañiz A, Procel P, Kawa E, Zhao Y, Tiringer U, et al. Strategy to mitigate the dipole interfacial states in (i)a-Si:H/MoO$_x$ passivating contacts solar cells. Prog Photovoltaics Res Appl 2021;29:391–400. https://doi.org/10.1002/pip.3381.

[9] Kanai K, Koizumi K, Ouchi S, Tsukamoto Y, Sakanoue K, Ouchi Y, et al. Electronic structure of anode interface with molybdenum oxide buffer layer. Org Electron 2010;11:188–94. https://doi.org/10.1016/j.orgel.2009.10.013.

[10] Vaněček M, Kočka J, Stuchlík J, Kožíšek Z, Štika O, Tříska A. Density of the gap states in undoped and doped glow discharge a-Si:H. Sol Energy Mater 1983;8:411–23. https://doi.org/10.1016/0165-1633(83)90006-0.

[11] Scirè D, Procel P, Gulino A, Isabella O, Zeman M, Crupi I. Sub-gap defect density characterization of molybdenum oxide: An annealing study for solar cell applications. Nano Res 2020;13:3416–24. https://doi.org/10.1007/s12274-020-3029-9.

[12] Gulino A, Condorelli GG, Fragalà I. Synthesis and spectroscopic characterisation of MoO 3 thin films. J Mater Chem 1996;6:1335–8. https://doi.org/10.1039/JM9960601335.

[13] Ederth J, Hoel A, Niklasson GA, Granqvist CG. Small polaron formation in porous WO3-x nanoparticle films. J Appl Phys 2004;96:5722–6. https://doi.org/10.1063/1.1804617.

[14] Dieterle M, Weinberg G, Mestl G. Raman spectroscopy of molybdenum oxides - Part I. Structural characterization of oxygen defects in MoO3-x by DR UV/VIS, Raman spectroscopy and X-ray diffraction. Phys Chem Chem Phys 2002;4:812–21. https://doi.org/10.1039/b107012f.

[15] Gulino A, Tabbì G. CdO thin films: A study of their electronic structure by electron spin resonance spectroscopy. Appl Surf Sci 2005;245:322–7. https://doi.org/10.1016/j.apsusc.2004.10.026.

[16] Colton RJ, Guzman AM, Rabalais JW. Photochromism and Electrochromism in Amorphous Transition Metal Oxide Films. Acc Chem Res 1978;11:170–6. https://doi.org/10.1021/ar50124a008.

[17] Reticcioli M. Polarons in Transition-Metal Oxides. In: Andreoni W, Yip S, editors. Comments Solid State Phys, vol. 1,

Cham: Springer International Publishing; 1968, p. 105–11. https://doi.org/10.1007/978-3-319-50257-1_52-1.

[18]   Austin IG, Mott NF. Polarons in crystalline and non-crystalline materials. Adv Phys 2001;50:757–812. https://doi.org/10.1080/00018730110103249.

[19]   Livage J. Small Polarons in Transition Metal Oxide Glasses. Glas. … Curr. Issues, Dordrecht: Springer Netherlands; 1985, p. 408–18. https://doi.org/10.1007/978-94-009-5107-5_34.